www.springer.com/41230
https://doi.org/10.1007/s41230-025-4157-3

Regional differences in mechanical properties of high-pressure vacuum casting AlSi10MnMg automotive rear longitudinal beam

Qing-hua Li[1, 3], *Heng Li[1, 3], Zhen Chai[2], Xiao-yong Zhu[3], and Yu-cheng Wu[1, 3]

1. School of Materials Science and Engineering, Hefei University of Technology, Hefei 230009, China

2. Wuhu Rayhoo Lightweight Technology Co., Ltd., Wuhu 241000, Anhui, China

3. Anhui Province Key Lab of Aerospace Structural Parts Forming Technology and Equipment, Hefei University of Technology, Hefei 230009, China

Abstract: The development of new energy vehicles and their lightweight requirements promote the application of one-piece die-casting integrated structural components. The dimensions of these castings are large, and the performance of different regions varies significantly. Therefore, ensuring the mechanical properties of key stress areas is particularly important. This work focuses on the rear longitudinal beam integrated structural component made from AlSi10MnMg alloy. The microstructure and mechanical properties of the die-casting and heat-treatment states in key stress areas were analyzed, considering the filling path. The results show that both the number and distribution of eutectic silicon, intermetallic compounds, and pores change significantly with an increase in distance from the filling path. As the filling path extends from 0 to 702 mm, the eutectic silicon content increases from 45.86% to 72.66%, leading to a reduction in elongation. The quantity and size of pores in the far-gate region increase compared to the near-gate region. Moreover, the micropores grow in the alloy after heat treatment. Following heat treatment, small-sized polygonal Al-Mg and Fe-Mn intermetallic compounds, measuring 2.5–7 μm, are concentrated in the far-gate region. Under the combined influence of these factors, both the tensile strength and elongation of the castings exhibit a decreasing trend as the distance from the gate increases. Research indicates that increasing the pressure injection rate and extending the holding time are primary strategies for enhancing the alloy's toughness, provided the alloy composition and vacuum level are controlled.

Keywords: AlSi10MnMg alloy; vacuum die casting; solidification simulation; microstructure; mechanical property

CLC numbers: TG146.21 **Document code:** A **Article ID:** 1672-6421(2026)04-544-11

1 Introduction

In recent years, many new energy vehicles have rapidly emerged, accelerating the promotion of structural lightness in the automotive industry[1, 2]. AlSi10MnMg is a common sub-eutectic aluminum-silicon alloy with excellent casting properties, high strength, and significant lightweight characteristics. Therefore, it is widely used in high-pressure vacuum casting for complex thin-walled structural components in automotive bodies[3, 4]. Conventional automotive rear longitudinal beams and shock absorber towers are made from steels and produced using cold stamping and welding technologies. According to our practices, the AlSi10MnMg thin-walled automotive structural components produced by high-pressure vacuum casting can achieve up to 35% weight reduction while maintaining mechanical properties.

However, there are regional differences in the mechanical properties of AlSi10MnMg high-pressure cast automotive thin-walled structural components. This phenomenon is predominantly observed in the distal and proximal regions relative to the gate within the same casting, particularly in structural components with dimensions exceeding 500 mm and a mass greater than 10 kg. The solidification of the alloy during the die-casting process causes large differences in cooling

***Heng Li**

Male, born in 1984, Ph. D. Research interests: theory and process of metal plastic forming, preparation and processing of high-strength and high-toughness non-ferrous alloys.

E-mail: liheng0205@hfut.edu.cn

Received: 2024-07-30; Revised: 2024-10-25; Accepted: 2024-11-15

rates and temperature gradients in different regions of large die-castings[5-7]. Additionally, differences in metal flow rate and pressure between near and far gate regions affect the consistency of casting mechanical properties[8]. Casting defects such as porosity, and coarse and inhomogeneity structure during solidification in vacuum die-casting remain significant challenges for further improving alloy performance. Insufficient toughness of the alloy in areas away from the gate system can result in cracks in the riveted joints of thin-walled structural components and the vehicle body. Vibration loading exposes these joints to periodic stress, accelerating fatigue damage and posing significant safety hazards. Therefore, studying the factors influencing the insufficient mechanical properties at the distal end of the filling path after die-casting is imperative.

Researchers have thoroughly investigated the link between casting defects and casting properties from various perspectives and methods. Niklas et al.[9] found that the elongation of the material decreased significantly with increasing porosity. Fractures occurred preferentially at the location of the largest pores, and the elongation was strongly correlated with the volume fraction of the largest pores[10]. With the continuous improvement of research methods, some scholars have used a combination of simulation and experiment to study the formation and evolution of pores during the casting process. Zhang et al.[11] proposed a coupled lattice LB-CA-FD model to simulate porosity formation during the solidification of binary sub-eutectic aluminum alloy dendrites. A link between porosity and secondary dendrite arms was found: the pores tend to grow in the spaces between the secondary dendrite arms. Cheng's team[12, 13] found that the cooling rate significantly affected the number, volume, and size of pores, further refining the link between secondary dendrite arms and porosity formation. Additionally, from a microstructure perspective, the effects of externally solidified crystals (ESCs) and β-Al_5FeSi iron-rich phases on the alloy's properties require attention. Jiao et al.[14] found that coarse ESCs precipitated from the liquid phase along the walls of the compression chamber during the slow injection velocity stage and were retained in the castings. These coarse structures promote large-sized shrinkage, increasing porosity within the casting, and significantly affecting mechanical properties. Researchers, including Jiao et al.[14], observed the morphology and distribution of iron-rich phases in AlSi10MnMg alloy using an electron microscope. Meanwhile, phase precipitation during the alloy solidification was predicted using the Thermal-Calc software. It is found that iron-rich phases in high-pressure vacuum casting AlSi10MnMg alloy exhibit various morphologies, including primary iron-rich phases (polyhedral (P-IMC) I, (P-IMC) II) and eutectic iron-rich phases (plate-like and fishbone-like). The larger polyhedral iron-rich phases become the sources of stress concentration, promoting microcrack formation and extension[15, 16].

This study integrates findings from previous literature by adopting the filling path as a central framework. It investigates how the spatial distribution of microstructure and pores influences the alloy's mechanical properties across different regions, with a tripartite analysis focusing on eutectic silicon morphology, iron-rich phase segregation, and porosity. The research utilizes automotive longitudinal beams manufactured via vacuum die-casting of AlSi10MnMg as the study objects. The solidification behavior of the alloy was simulated using Pandat software. Sampling and characterization of different regions near and far from the gate of the longitudinal beam filling paths were carried out at the microscopic level, to analyze the main influencing factors causing regional differences in the mechanical properties of longitudinal beam integrated structural components. This work can provide guidance for solving such performance differences.

2 Experiment

The raw materials included AlSi10MnMg ingot, pure magnesium, and Al-Sr intermediate alloy. The AlSi10MnMg ingot was placed in a melting furnace, heated to 710 °C to completely melt. The aluminum liquid was then heated to 720 °C and transferred to a ladle, where pure magnesium and Al-Sr intermediate alloy were added and stirred. Nitrogen gas with 99.9% purity was used for degassing and dross removal by stirring with a graphite rotor for 10 min. The aluminum liquid was then poured into a 4,500 t cold chamber die-casting machine for the die-casting experiments. The main die-casting process parameters used in this work were as follows: aluminum liquid temperature of 680 °C, initial mold temperature of 180 °C, high injection speed of 5.28 $m \cdot s^{-1}$, vacuum degree of about 40 mbar, and casting pressure of 60 MPa. After die-casting, the structural components were removed from the mold, immediately cooled in water, and subsequently subjected to trimming, deburring, and polishing processes. Subsequently, the castings underwent a T7 heat treatment process: solid solution temperature of 485±5 °C, solid solution time of 80±5 min; aging temperature of 230±5 °C, and aging time of 160±5 min. Structural components were air quenched for 10 min after solid solution treatment. The chemical compositions of the alloy were measured using a direct-reading spectrometer (QLH-76-001), as shown in Table 1.

Samples for performance testing were cut from the same batch of die-cast and T7 heat-treated castings. The specific sampling location, gating system, and overflow system are shown in Fig. 1. The sampling locations were sequentially numbered from 1 to 4 based on their proximity to the near-gate and far-gate regions along the filling path. The distances from the sampling locations

Table 1: Chemical compositions of experimental alloy (wt.%)

Elemental	Si	Fe	Cu	Mn	Mg	Ti	Sr	V	Al
Nominal	9.5–11.5	0–0.12	0–0.03	0.6–0.8	0.25–0.35	0.05–0.1	0.02–0.03	0–0.03	Bal.
Measured	10.75	0.0664	0.0089	0.675	0.288	0.0658	0.0268	0.0153	Bal.

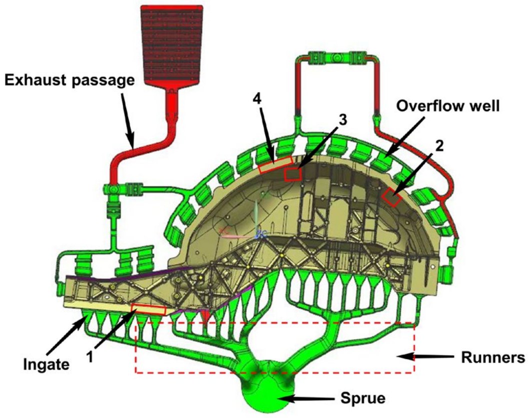

Fig. 1: Distribution of ingate, overflow well, exhaust passage, and sampling locations (1, 2, 3, 4)

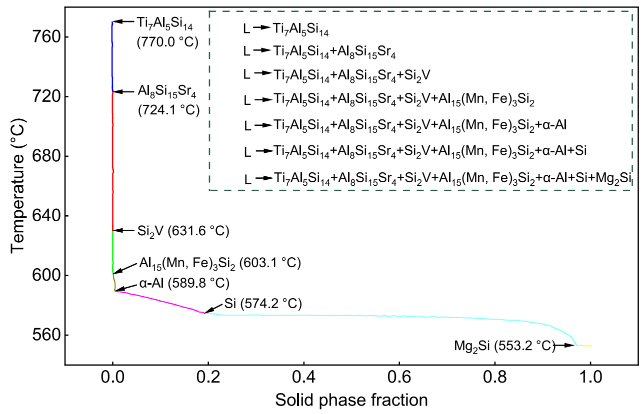

Fig. 2: Solidification curve of AlSi10MnMg alloy

(Positions 1, 2, 3, and 4) to the gate were 0, 538, 604, and 702 mm, respectively. Regarding wall thickness uniformity, the wall thickness at the near-gate position is 3.5 mm (Position 1), whereas the transition area between the near-gate and far-gate regions exhibits a reduced thickness of 2.5 mm (corresponding to Positions 2, 3, and 4). The gating system was set at the bottom of the lower sill and the longitudinal beam. The overflow system was set on the outside of the upper sill and wheel cover edge. After sampling, the tensile specimens and metallographic specimens were cut using the DK7725Z precision EDM wire cutting machine. The tensile specimens were tested on an AGS-X-10KNXD mechanical properties tester. The surfaces of the metallographic samples were treated separately using different types of sandpapers as well as standard ratios of Keller's reagent. Finally, the metallographic and microstructures of different specimens were observed using a Zeiss Axiolab 5 metallographic microscope and a cold field emission scanning electron microscope (SU8020).

3 Results and discussion

3.1 Solidification simulation of AlSi10MnMg alloys

To explore the intrinsic factors affecting the mechanical properties of longitudinal beams, thermodynamic calculations and microstructural characterization were performed. The phase evolution during the solidification of AlSi10MnMg alloy was simulated. The primary elements Al, Si, Mn, and Mg form the Fcc (Al), diamond (Si), $Al_{15}(Mn, Fe)_3Si_2$, and Mg_2Si phase, respectively. Trace elements Ti, Sr, and V form the $Ti_7Al_5Si_{14}$, $Al_8Si_{15}Sr_4$, and Si_2V phase, respectively.

According to the solidification curve of the alloy (Fig. 2), the precipitation temperatures of the $Ti_7Al_5Si_{14}$ phase and $Al_8Si_{15}Sr_4$ phase are 770.0 °C and 724.1 °C, respectively. During the actual melting and heat preservation, the liquid aluminum temperature is kept at 720±20 °C, and during die-casting, it is 710±10 °C. Therefore, the $Ti_7Al_5Si_{14}$ phase and $Al_8Si_{15}Sr_4$ phase are preferentially precipitated in the injection chamber before die-casting production. During solidification, the Si_2V, $Al_{15}(Mn, Fe)_3Si_2$, α-Al, Al-Si eutectic, and Mg_2Si phase precipitate successively. Among them, the $Al_{15}(Mn, Fe)_3Si_2$ phase, α-Al, and Al-Si eutectic constitute the main architecture of the alloy. Figure 2 illustrates the precipitation temperatures of each phase during the solidification of AlSi10MnMg alloys and the precipitation reactions at each stage.

3.2 Eutectic silicon segregation

Figures 3(a) and (c) show the EBSD diffraction quality maps (band contrast) at Positions 1 and 3, respectively. The α-Al matrix exhibits high contrast with distinct microstructural features, whereas the eutectic silicon regions exhibit a darker contrast. Preliminary indications are that defects or strains in the alloy are concentrated in the eutectic silicon region. The grain size distributions at Positions 1 and 3 were analyzed using the EBSD-IPF map [Figs. 3(b) and (d)]. Differences in grain size distribution can be observed between Position 1 (near gate region) and Position 3 (far gate region). The statistical results are shown in Figs. 3(f) and (g). The average grain size in Position 1 (13.8429 μm) is larger than that in Position 3 (11.3061 μm). From a casting design geometry perspective, the longitudinal beam features many small reinforcement modules at the near-gate region, making the geometry more complex. Such complex geometry or small structural features may obstruct the melt flow, resulting in the accumulation of large-sized pre-crystallized structures at the near-gate region. The solidification speed of the thin-walled zone is significantly higher than the thick-walled zone, leading to the differences in grain size. When the casting wall thickness changes abruptly, such as transitioning from thick to thin, it results in uneven melt flow, leading to the formation of coarse structures. This can be observed in the subsequent metallographic photographs. This shows that the α-Al matrix in the die-cast state shows a typical dendritic structure. Moreover, the α-Al phase mainly consists of a larger-sized (α-Al)I phase and a smaller-sized (α-Al)II phase, with the coarse (α-Al)I phase primarily distributed in Position 1.

Figures 4(a)–(d) show the local orientation difference maps (LAM maps) at Positions 1 and 3. The different color distributions in these figures represent varying degrees of orientation differences, indirectly reflecting the distribution of dislocation density and stress at each position. Figures 4(a) and (c) show that the blue color, symbolizing smaller orientation differences, is mostly distributed within the α-Al matrix, while

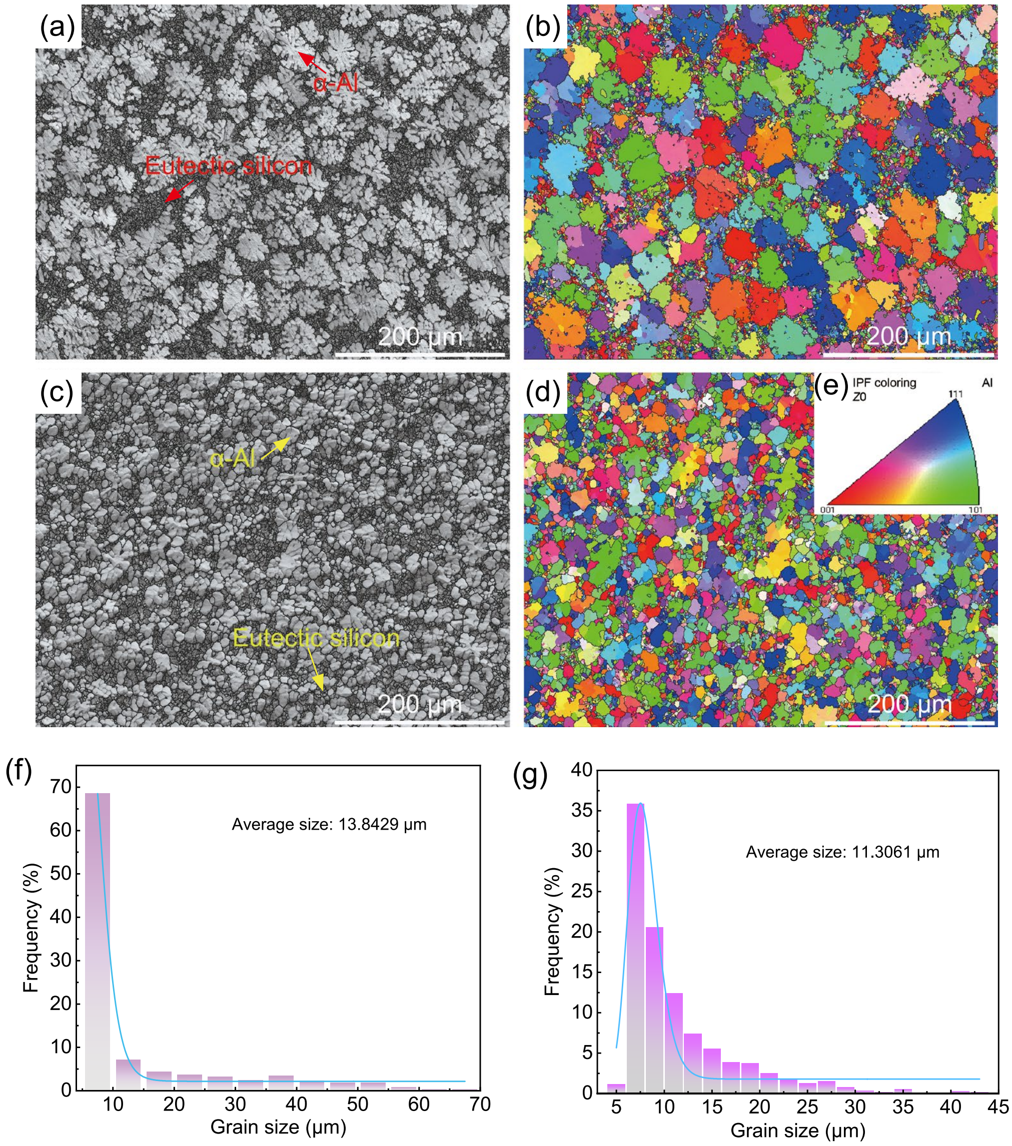

Fig. 3: EBSD characterization results for Positions 1 (a, c, f) and 3 (b, d, g): (a, c) band contrast map; (b, d) IPF antipodal map in the *Z*-axis direction; (e) color code of (b, d); (f, g) grain size distribution

the yellow-green color, indicating larger orientation differences, is mainly distributed in the eutectic silicon regions. This suggests that the dislocation density and stress in the alloy are primarily concentrated in the region of fine eutectic structures. Comparing the two LAM maps and their corresponding legends, it can be found that the yellow-green color distribution at Position 3 is denser and accounts for a larger proportion.

During metallographic observation of the cast specimens, differences in eutectic silicon content are noticed in the near- and far-gate regions of the filling paths. The distribution of the α-Al matrix is denser in the near-gate region than that in the far-gate region, and the content of eutectic silicon in the casting increases with an increase in distance from the gate. In particular, varying degrees of eutectic silicon segregation are found in Positions 3 and 4. As statistically shown in Figs. 4(e) to (h), the eutectic silicon content increases from 45.86% to 72.66% as the distance between the sampling position and the gate increases. This suggests that the high solidification rate in the distal region leads to rapid solidification of some inhomogeneous structures, forming eutectic silicon segregation regions.

3.3 Surface and fracture characterization

In Fig. 5(a), several spheroidal bright particles are observed, exhibiting a diffuse distribution across both the α-Al matrix and the eutectic silicon. In Fig. 5(b), the size of these spherical dispersed phases varies from 30 to 100 nm according to the local magnification. EDS characterization reveals that these spheroidal dispersed phases are $Ti_7Al_5Si_{14}$ precipitated at high temperatures. The diffuse distribution of these fine particles contributes to the enhancement of the deformation resistance of the matrix, thus increasing the hardness. According to the solidification simulation results discussed above, three high-temperature phases, $Ti_7Al_5Si_{14}$, $Al_8Si_{15}Sr_4$, and Si_2V, are predicted to precipitate prior to the formation of the Fe-rich phase. However, during actual microstructural characterization of the alloy, only small and sparsely distributed $Ti_7Al_5Si_{14}$ phases are observed. This discrepancy may be attributed to the extremely low concentrations of Sr and V in the alloy.

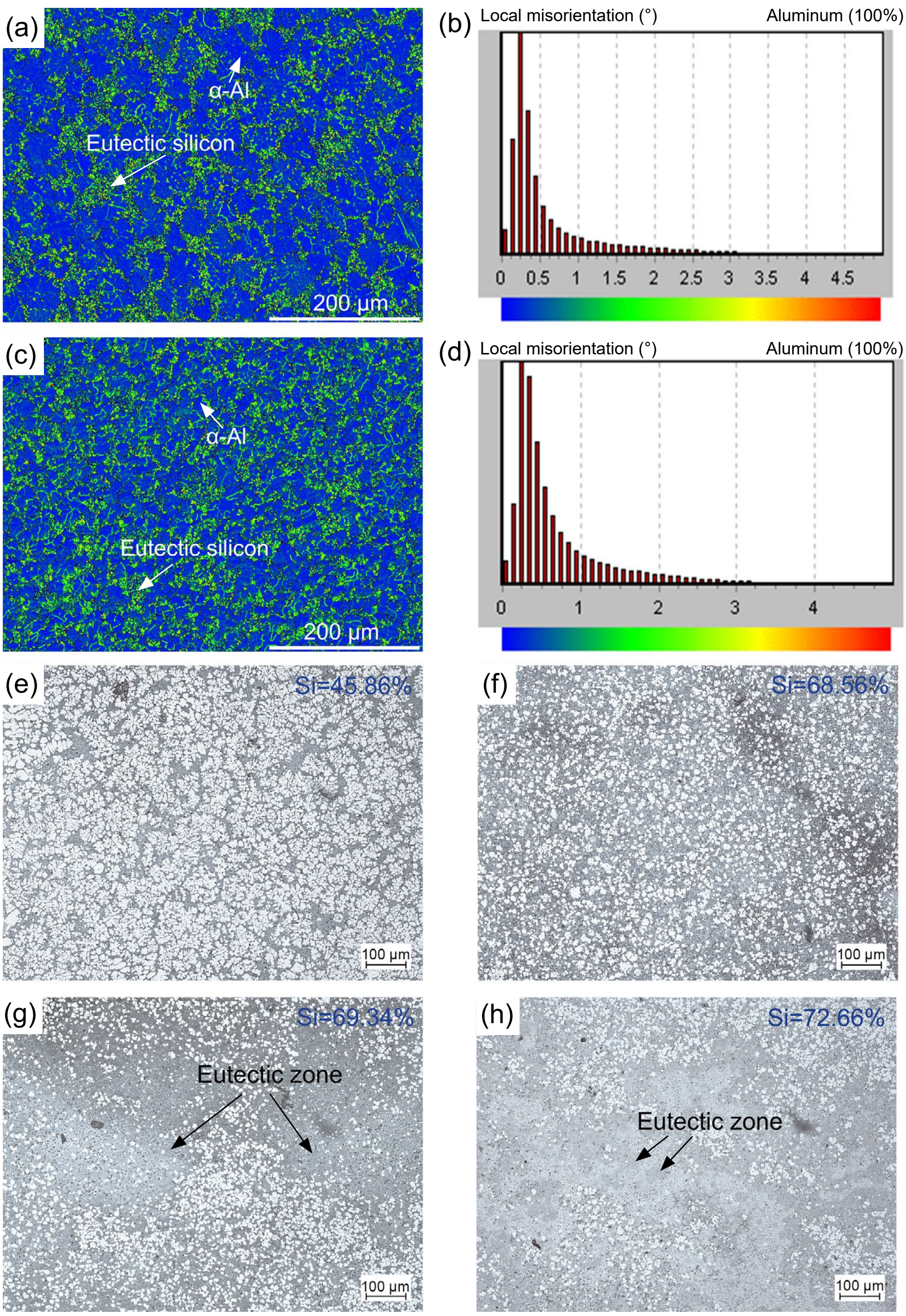

Fig. 4: LAM maps for Positions 1 and 3 (a, c), local misorientation for (a, c), respectively (b, d), and localized deviation of eutectic silicon at the distal end of the casting filling paths (e)–(h)

Figure 6 shows the surface SEM images of the four sampling positions in the die-casting state. Most of the eutectic silicon is distributed with short rods and worms, with a few appearing as spheres or particles. Research indicates that the adsorption of Sr on the surface of eutectic silicon inhibits its growth, preventing the formation of elongated eutectic silicon plates[17]. Comparing Figs. 6(a) and (c), it is evident that there are many micropores located at Positions 3 and 4. These micropores exist as defects in the material and can easily become initiation points for cracks. When the material is subjected to external loads, the pores will exacerbate crack extension and reduce the plastic deformation capacity and toughness of the material.

Figure 7 shows the SEM characterization of Positions 1 and 3 after heat treatment. It is evident in Figs. 7(a) and (b) that after heat treatment, the eutectic silicon melts at high temperatures, and the degree of spheroidization increases. Comparing the size of eutectic silicon in the die-cast state (Fig. 6), the eutectic silicon undergoes obvious coarsening after heat treatment. After T7 heat treatment, the grain recrystallization and spheroidization and coarsening of eutectic silicon that occur during the heat treatment process may reduce the strength and increase the elongation of the alloy. This is because that grain

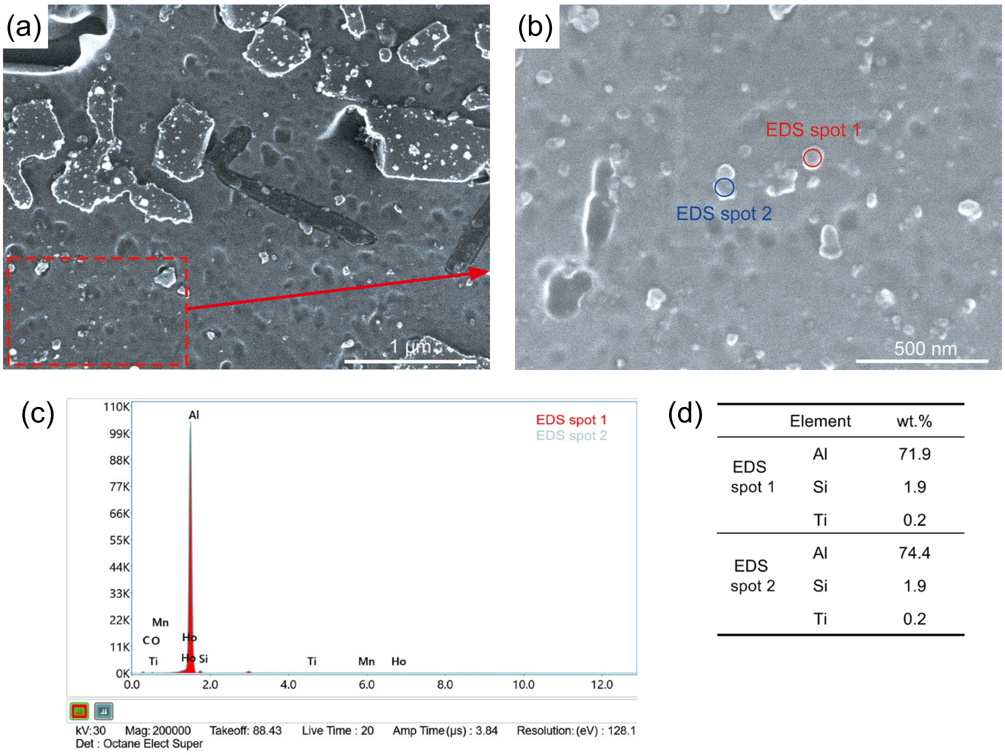

	Element	wt.%
EDS spot 1	Al	71.9
	Si	1.9
	Ti	0.2
EDS spot 2	Al	74.4
	Si	1.9
	Ti	0.2

Fig. 5: Distribution of $Ti_7Al_5Si_{14}$ phase in the alloy (a); local magnification (b); EDS characterization results of $Ti_7Al_5Si_{14}$ phase (c, d)

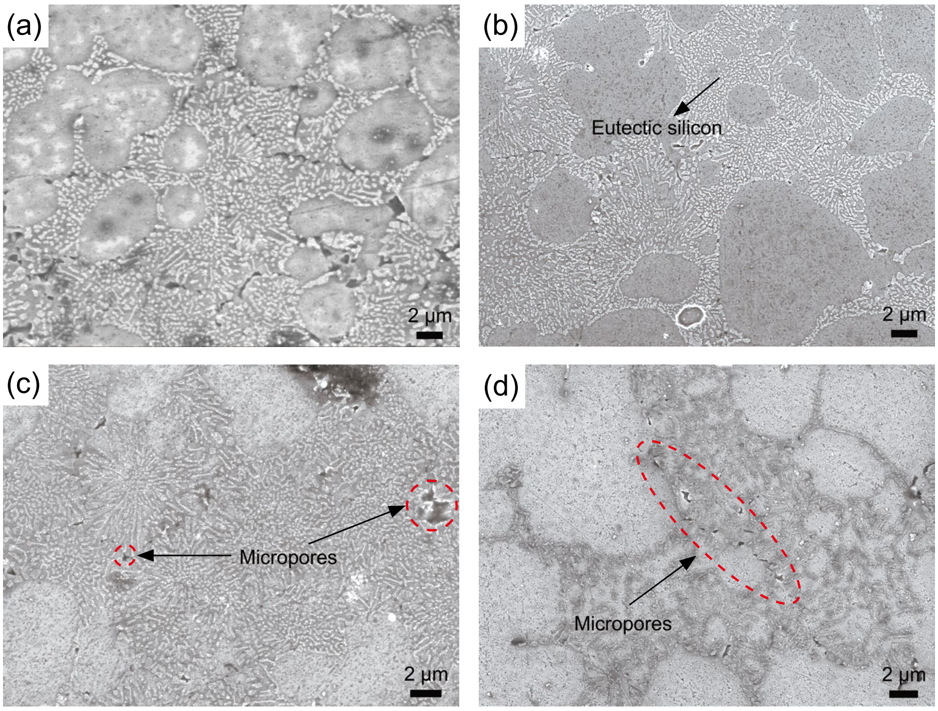

Fig. 6: SEM images of the longitudinal beam in the die-cast state at Positions 1 (a), 2 (b), 3 (c), and 4 (d)

recrystallization leads to a reduction in the grain boundaries of the alloy, weakening the hindering effect of the grain boundaries on the dislocation movement. This results in reduced strength and increased elongation of the alloy. Meanwhile, the spheroidization of eutectic silicon during heat treatment enhances the continuity of the matrix, leading to an increase in the elongation of the alloy. Furthermore, the coarsening of eutectic silicon also negatively affects the strength of the alloy. Slightly larger-sized oxidized inclusions can be observed at Position 3 in Fig. 7(b). These oxidized inclusions are formed in the grain boundaries and pores of the alloy. These oxides lead to stress concentration at the grain boundaries and pores, reducing the strength and deformation resistance of the alloy. Inclusions can also provide crack initiation points, further reducing the strength of the alloy. Such casting defects are a major cause of poor material properties. In addition, many Mn-rich phases

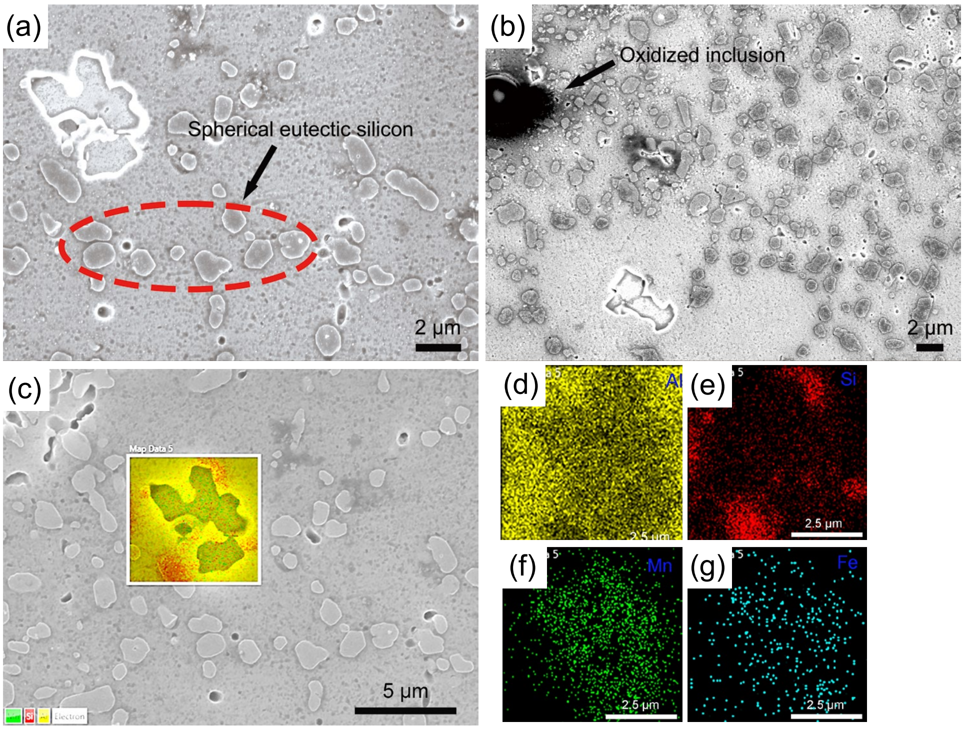

Fig. 7: SEM images of the alloy after T7 heat treatment at Positions 1 (a) and 3 (b), and $Al_{15}(Mn, Fe)_3Si_2$ phase energy spectra (c)–(g)

with bright edges are found in each sampling position before and after heat treatment, which is characterized by EDS as $Al_{15}(Mn, Fe)_3Si_2$ phases [Fig. 7(c)].

3.4 Effects of porosity

During the observation of the metallographic microstructure of AlSi10MnMg alloy in die-cast and heat-treated states, it is found that the size and distribution of pores in the alloy followed a certain pattern, as shown in Fig. 8. In Fig. 8(b), a few porosities can be observed, most of which are smaller than 5 μm. Only a limited number of larger pores, approximately 10 μm in size, are present. In contrast, both the number and size of defects in Figs. 8(c) and (d) increase. On the one hand, large-sized gas shrinkage porosity is formed by gas entrapment and solidification shrinkage during the die-casting mold-filling process. On the other hand, shrinkage and small-sized pores are enriched near grain boundaries as well as in eutectic silicon regions. This leads to continuous large-sized cracks formed by stress concentration under the effect of intense cooling.

The change rule of porosity can be clearly observed in Fig. 8. Firstly, the porosity in the same sample increases as the distance to the gate increases. This is caused by the large difference in temperature gradient between the near- and far-gate regions. The temperature gradient in the far-gate region is relatively high, and the rapid cooling rate of the casting prevents the residual gas from being discharged in time during the filling process. As a result, large pores and other defects tend to form in this area. At the same time, the higher cooling rate leads to uneven

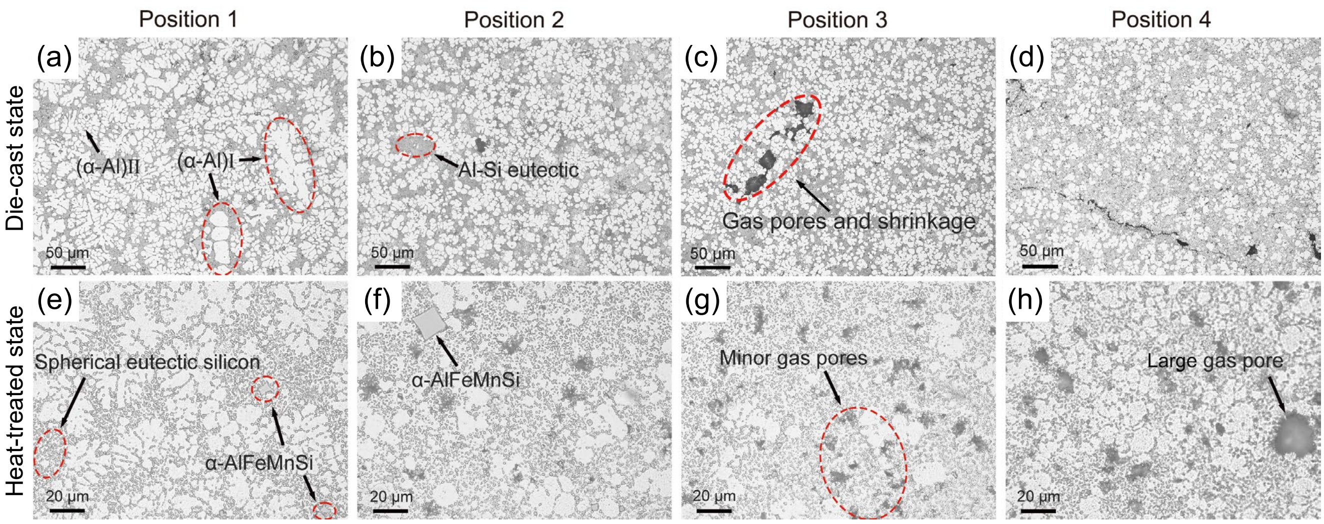

Fig. 8: Metallographic structures of longitudinal beams in die-cast (a to d) and heat-treated (e to h) states at each sampling position

contraction of castings, resulting in stress concentration within the casting, negative affecting the mechanical properties of the alloy. Secondly, the size and number of pores in the casting increase after heat treatment. This phenomenon is attributed to the microporosity present in the casting expanding thermally during the T7 heat treatment. Consequently, this leads to an increase in both the size and quantity of large pores within the casting, which negatively impacts the alloy's strength. After heat treatment, eutectic silicon continuously dissolves and breaks, transforming from the short rod and worm-like structures in the as-cast state into spherical particles. On the one hand, a portion of the eutectic silicon is dissolved back into the aluminum matrix, and the spheroidization of the eutectic silicon enhances the continuity of the aluminum matrix. This greatly improves the plasticity and toughness of the alloys. On the other hand, the uniformly distributed spherical and particulate eutectic silicon plays a role in dispersion strengthening. Comprehensively, the following conclusions can be drawn from the above observations on the state and distribution of pores in different sampling positions before and after heat treatment: Porosity is an important factor contributing to the difference in performance between the near- and far-gate regions of the casting's filling paths.

3.5 Mechanical properties

Figure 9(a) shows the mechanical properties of the alloy in the die-casting state and heat-treatment state for Positions 1 to 4. Overall, the yield strength of the alloys at the four sampling positions on the longitudinal beam integrated structural component changes little before and after heat treatment. The yield strength of the alloys at the four sampling positions in the die-casting state (130–145 MPa) is slightly higher than that after heat treatment (120–130 MPa). The primary differences can be summarized in two key aspects. Firstly, notable differences are observed in the tensile strength and elongation of the alloys across various sampling locations in the as-cast and heat-treated conditions. Secondly, the variation in elongation among the four sampling positions in the two states also differs significantly, indicating position-dependent mechanical behavior. It is observed from Fig. 9(a) that the tensile strength at each sampling position decreases by 20%–30% compared with the die-casting state. However, the elongation is about twice as that of the die-casting state. The tensile strength and elongation of the alloys at Positions 1 and 2 in both states are better than those at Positions 3 and 4. In other words, the tensile strength and elongation of the alloys decrease as the distance from the gate system increases.

3.6 Fracture characterization

Figures 10 and 11 show the tensile fracture morphology of the casting at Positions 1 and 4 before and after heat treatment. A comparison of the fracture morphology before and after heat treatment reveals differences in the distribution of ductile dimples at the fracture. The number of ductile dimples at the fracture surface after heat treatment is greater than the die-casting state, and their size is also relatively larger. The size of pores at the fracture surface of Position 4 is larger and the number of pores is greater in both states. The cracks are mainly concentrated at the eutectic silicon. Many cleavage planes are observed in Fig. 10(d). Thus, it can be determined that the fracture form at Position 1 under die-cast state is a mixed ductile-brittle fracture, while that at Position 4 exhibits a brittle fracture. In the heat-treated state, the number of ductile dimples at the fracture surface is high and uniformly sized. However, with an increase in distance from the gate, both the size and density of the pores increase. The fracture form of the alloy gradually transitions from ductile fracture to mixed ductile-brittle fracture.

Figure 11(b) shows the SEM morphology of the fracture surface at Position 4 after heat treatment. A certain amount of intermetallic compounds are observed at the bottom of the fracture ductile dimples, with sizes ranging from 2.5 to 7 μm. These intermetallic compounds are rarely seen in the fracture profile of specimen at Position 1. Spectroscopic analysis determines that they are mainly Al-Mg and Fe-Mn phases. These intermetallic compounds are usually hard and brittle, and are prone to fracture under stress, thus reducing the overall toughness of the alloy. In addition, the presence of intermetallic compounds may lead to embrittlement in the

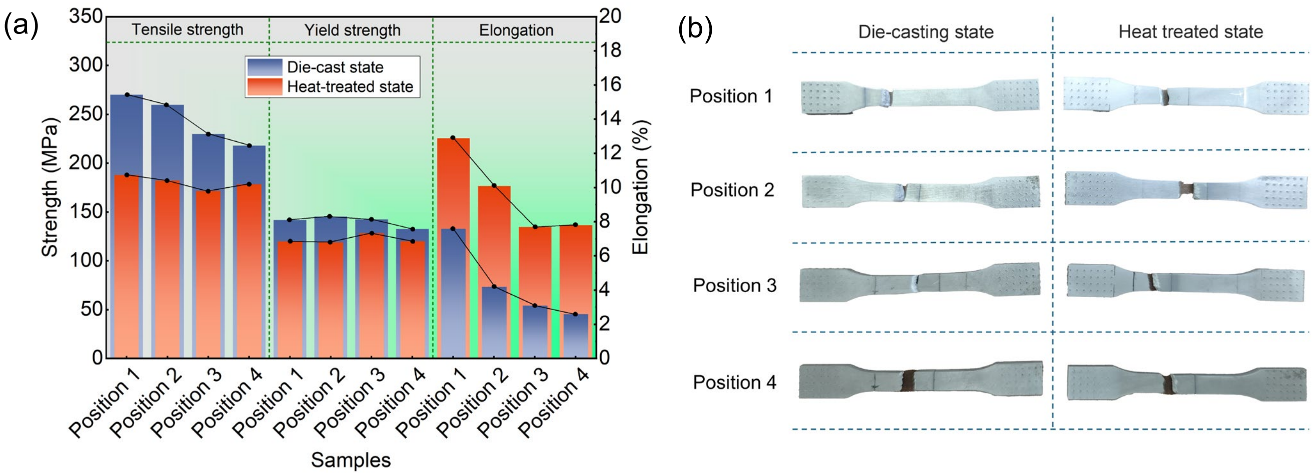

Fig. 9: Trend of mechanical properties before and after heat treatment (a), and tensile specimens used for the experiment (b)

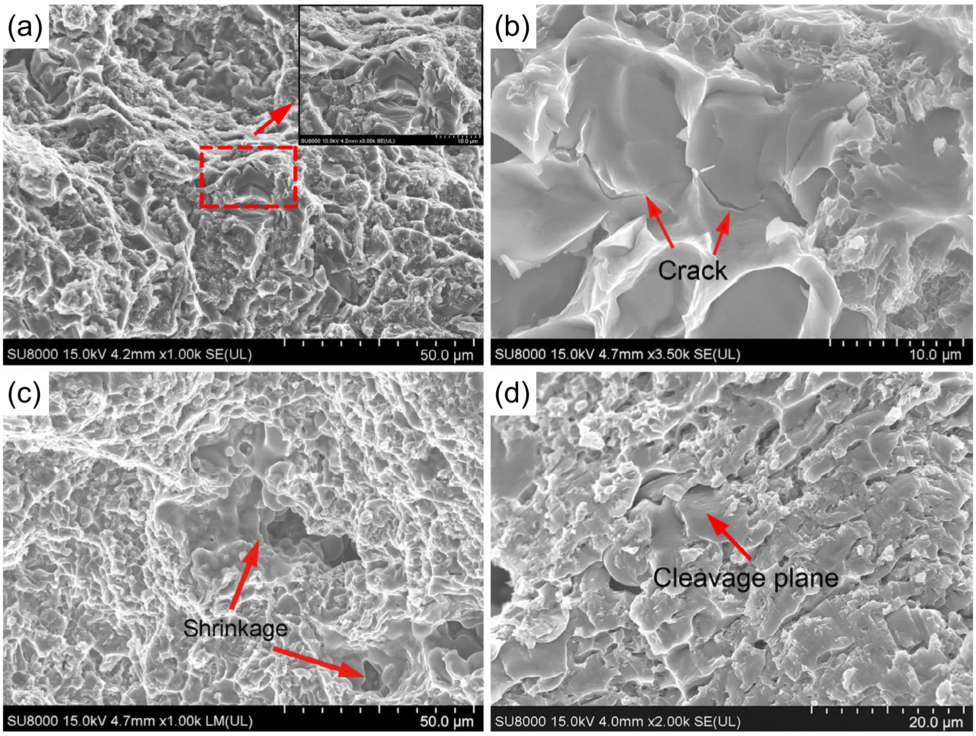

Fig. 10: Fracture morphology in die-casting state: (a, b) Position 1; (c, d) Position 4

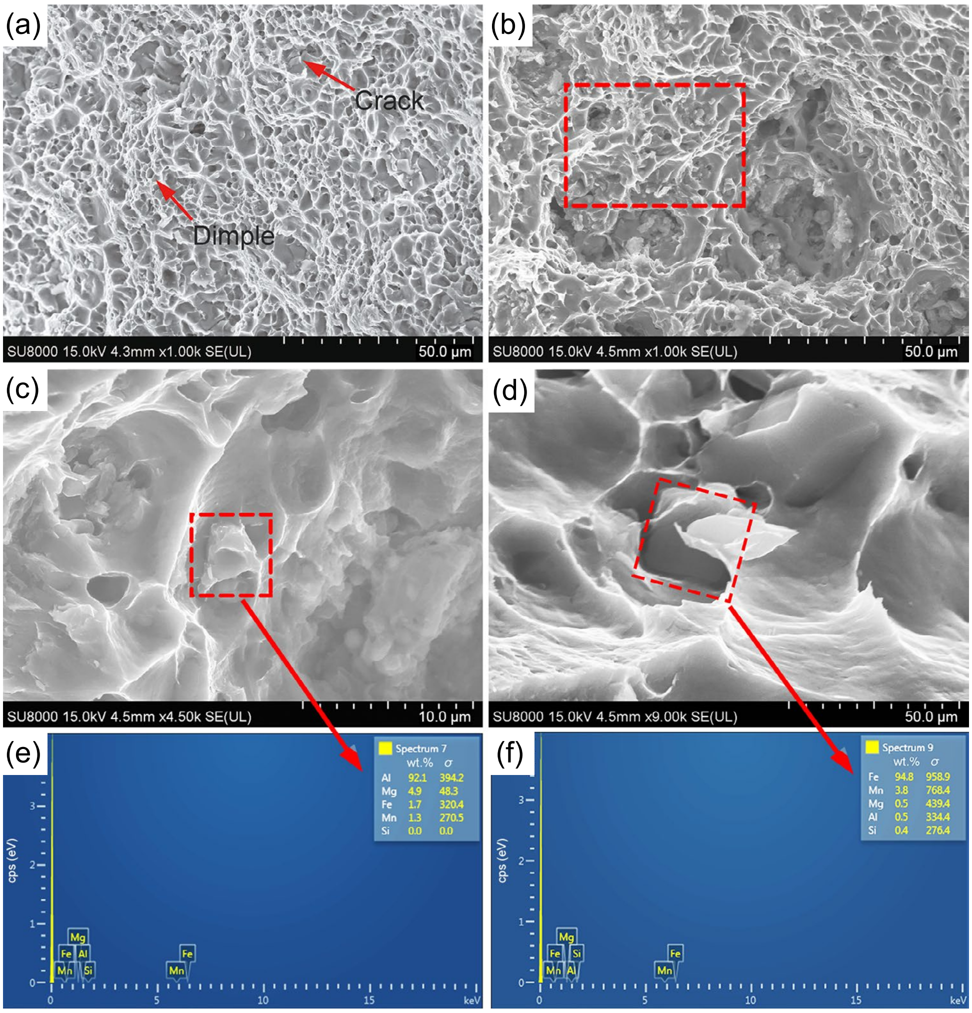

Fig. 11: Fracture morphology in heat-treatment state: (a) Position 1; (b) Position 4; (c, d) localized magnification of intermetallic compound observed at Position 4; (e, f) EDS characterization results of precipitated phase at Position 4

grain boundary region of the alloy, further deteriorating the toughness performance of the alloys.

In summary, the regional variations in the mechanical properties of the longitudinal beams are determined by a combination of the amount and distribution of eutectic silicon segregation, porosity, and intermetallic compounds. As shown in Figs. 4 and 8, both the eutectic silicon segregation and the number of porosities in the alloy intensify as the distance from the gate increases. In Fig. 11, a large number of brittle intermetallic compounds enrich at the distal end. According to previous research, the tensile strength and yield strength of aluminum-silicon alloys typically increase with increasing silicon content, while the elongation decreases[18-21]. However, the result of the actual mechanical property tests in this work shows the different trend. That is, as the distance from the gate increases in the die-casting state, the tensile strength of the alloy shows a decreasing trend as the distal eutectic silicon content rises. Therefore, eutectic silicon segregation affects the homogeneity of the distal microstructure of the casting, resulting in reduced distal strength. After heat treatment, the residual stresses within the casting are eliminated, and the spheroidization of eutectic silicon enhances the continuity of the matrix. The strength of the heat-treated castings stabilizes in both distal and proximal regions, but elongation still decreases as the distance from the sprue increases. Distal eutectic silicon segregation and the enrichment of small-sized intermetallic compounds remain challenging to resolve due to the casting geometry. However, porosity in the casting can be minimized by optimizing die-casting process parameters. Research has shown that under the premise of determined alloy composition and vacuum level, increasing the pressure injection speed and holding time can reduce the porosity in the alloy and improve its toughness[22]. Accordingly, optimizing the die-casting process to further reduce casting defects such as porosity in the alloy remains the main direction for future enhancement of alloy performance.

4 Conclusions

The main reasons for regional differences in mechanical properties along the filling path of high-pressure vacuum casting AlSi10MnMg alloys were investigated utilizing microstructural characterization and Pandat simulation. The conclusions can be drawn as follows:

(1) The α-Al matrix is denser in the near-gate region of the filling path than that in the far-gate region. As the distance from the gate increases, eutectic silicon content rises from 45.86% to 72.66%, leading to the formation of many eutectic silicon segregations due to rapid solidification of inhomogeneous structures.

(2) With an increase in distance from the gate, both the number and size of pores in the casting increase. During heat treatment, micropores grow, negatively impacting the strength of casting.

(3) Polygonal Al-Mg and Fe-Mn metal compounds, with a size ranging from 2.5 to 7 μm, concentrate at the distal end of the filling paths of the heat treated alloy. This may lead to embrittlement in the grain boundary region of the alloy, adversely affecting casting's toughness.

(4) The regional variations in the mechanical properties of longitudinal beams are influenced by the combined effects of eutectic silicon segregation, porosity, and intermetallic compounds. The tensile strength and elongation of the alloy decrease with increasing distance from the gate.

Acknowledgments

The authors acknowledge the Anhui Provincial Development and Reform Commission Innovation Project (Grant No. JZ2022AFKJ0032), and the project of Key Laboratory of Advanced Functional Materials and Devices of Anhui Province (Grant No. PA2025GDSK0053).

Conflict of interest

The authors declare that they have no known competing financial interests or personal relationships that could have appeared to influence the work reported in this paper.

References

[1] Guo X P, Zhang X Y, Dong J Q, et al. Optimal allocation of urban new energy vehicles and traditional energy vehicles considering pollution and cost. Environment Development and Sustainability, 2024, 26(3): 6007–6026.

[2] Zhao X, Wang P, Yang Y, et al. Effect of artificial aging treatment on the mechanical properties and regulation of precipitated phase particles of high-pressure die-cast thin-wall AlSi10MnMg longitudinal carrier. Materials, 2023, 16(12): 4369.

[3] Ahn C, Jo I, Ji C, et al. Creep behavior of high-pressure die-cast AlSi10MnMg aluminum alloy. Materials Characterization, 2020, 167: 110495.

[4] Jiao X Y, Zhang W, Liu X Y, et al. The characterization of porosity and its relationship with externally solidified crystal in a high-pressure die-cast AlSi10MnMg alloy via a laboratory CT technique. Materials Letters, 2023, 335: 133807.

[5] Hung C H, Chu C W, Chang T L, et al. Effect of focal spot size on AlSi10Mg alloy parts fabricated by laser powder bed fusion: Process window, mechanical properties, and microstructure. Journal of Alloys and Compounds, 2024, 977: 173338.

[6] Chiang K T, Liu N M, and Tsai T C. Modeling and analysis of the effects of processing parameters on the performance characteristics in the high pressure die casting process of Al-Si alloys. International Journal of Advanced Manufacturing Technology, 2009, 41(11–12): 1076–1084.

[7] Yu J M, Wanderka N, Rack A, et al. Influence of impurities, strontium addition and cooling rate on microstructure evolution in Al-10Si-0.3Fe casting alloys. Journal of Alloys and Compounds, 2018, 766: 818–827.

[8] Jiao X Y, Wang P Y, Liu Y X, et al. Effect of shot speeds on the microstructural framework and abnormal eutectic bands in a high pressure die casting hypoeutectic AlSi10MnMg alloy. Journal of Materials Processing Technology, 2024, 326: 118312.

[9] Niklas A, Orden S, Bakedano A, et al. Effect of solution heat treatment on gas porosity and mechanical properties in a die cast step test part manufactured with a new AlSi10MnMg(Fe) secondary alloy. Materials Science and Engineering: A, 2016, 667: 376–382.

[10] Liu R X, Zheng J, Godlewski L, et al. Influence of pore characteristics and eutectic particles on the tensile properties of Al-Si-Mn-Mg high pressure die casting alloy. Materials Science and Engineering: A, 2020, 783: 139280.
[11] Zhang Q Y, Sun D K, Pan S Y, et al. Microporosity formation and dendrite growth during solidification of aluminum alloys: Modeling and experiment. International Journal of Heat and Mass Transfer, 2020, 146: 118838.
[12] Cheng G, Ridgeway C D, Cinkilic E, et al. Predicting gas and shrinkage porosity in solidification microstructure: A coupled three-dimensional cellular automaton model. Journal of Materials Science & Technology, 2020, 49: 91–105.
[13] Gu C, Lu Y, Luo A A. Three-dimensional visualization and quantification of microporosity in aluminum castings by X-ray micro-computed tomography. Journal of Materials Science & Technology, 2021, 65: 99–107.
[14] Jiao X Y, Zhang Y F, Wang J, et al. Characterization of externally solidified crystals in a high-pressure die-cast AlSi10MnMg alloy and their effect on porosities and mechanical properties. Journal of Materials Processing Technology, 2021, 298: 117299.
[15] Jiao X Y, Liu C F, Guo Z P, et al. The characterization of Fe-rich phases in a high-pressure die cast hypoeutectic aluminum-silicon alloy. Journal of Materials Science & Technology, 2020, 51: 54–62.
[16] Jiao X Y, Liu Y X, Wang J, et al. The microstructure characteristics and fracture behavior of the polyhedral primary iron-rich phase and plate-shaped eutectic iron-rich phase in a high-pressure die-cast AlSi10MnMg alloy. Journal of Materials Science & Technology, 2023, 140: 201–209.
[17] Timpel M, Wanderka N, Schlesiger R, et al. The role of strontium in modifying aluminium-silicon alloys. Acta Materialia, 2012, 60(9): 3920–3928.
[18] Ali M M, Omran A N M, and Mohamed M A. Prediction the correlations between hardness and tensile properties of aluminium-silicon alloys produced by various modifiers and grain refineries using regression analysis and an artificial neural network model. Engineering Science and Technology, an International Journal, 2021, 24(1): 105–111.
[19] Haque M M. Effect of silicon on strength and fracture surfaces of aluminium-silicon casting and heat treated alloys. Putra I S, Switzerland: Key Engineering Materials, 2006, 306–308: 893–898.
[20] Wu J H, Zhang H L, Zhang Y, et al. Enhanced mechanical properties in Al/diamond composites by Si addition. Rare Metals, 2016, 35(9): 701–704.
[21] Kim Y M, Kang D S, Hong S K, et al. Influence of variation in the silicon content on the silicon precipitation in the Al-Si binary system. Journal of Thermal Analysis and Calorimetry, 2017, 128(1): 107–113.
[22] Adamane A R, Arnberg L, Fiorese E, et al. Influence of injection parameters on the porosity and tensile properties of high-pressure die cast Al-Si alloys: A review. International Journal of Metalcasting, 2015, 9(1): 43–53.